Polyol-Made Spinel Ferrite Nanoparticles—Local Structure and Operating Conditions: NiFe$_2$O$_4$ as a Case Study

T. Gaudisson[1], S. Nowak[1], Z. Nehme[2], N. Menguy[3], N. Yaacoub[2], J.-M. Grenèche[2] and S. Ammar[1]*

[1]ITODYS, Université de Paris, CNRS (UMR-7086), Paris, France, [2]IMMM, Le Mans Université, CNRS (UMR-6283), Le Mans, France, [3]IMPMC, Sorbonne Université, CNRS (UMR-7590), Paris, France

We report the effect of a polyol-mediated annealing on nickel ferrite nanoparticles. By combining X-ray fluorescence spectroscopy, X-ray diffraction, and ^{57}Fe Mössbauer spectrometry, we showed that whereas the as-prepared nanoparticles (NFO) are stoichiometric, the annealed ones (a-NFO) are not, since Ni^0-based crystals precipitate. Nickel depletion from the spinel lattice and reduction in the polyol solvent are accompanied with an important cation migration. Indeed, thanks to Mössbauer hyperfine structure analysis, we evidenced that the cation distribution in NFO departs from the thermodynamically stable inverse spinel structure with a concentration of tetrahedrally coordinated Ni^{2+} of 20 wt-% (A sites). After annealing, and nickel demixing, originated very probably from the A sites of NFO lattice, the spinel phase accommodates with cation and anion vacancies, leading to the (Fe$^{3+}_{0.84}$□$_{0.16}$)$_A$ [Ni$^{2+}_{0.80}$Fe$^{3+}_{1.16}$□$_{0.04}$]$_B$O$_{4-0.20}$ formula, meaning that the applied polyol-mediated treatment is not so trivial.

Keywords: ferrite nanoparticles, polyol process, local structure analysis, polyol-mediated annealing, ^{57}Fe Mossbauer spectrometry

INTRODUCTION

Spinel ferrites are an old class of functional ceramic materials. They had attracted much interest since Néel's discovery of ferrimagnetism and antiferromagnetism in 1948 (Néel, 1948). Due to their high resistivity and the tailorability of their magnetic properties as a function of their chemical composition and local structure, they have been considered for a large number of electromagnetic applications: magnetic sensors, permanent magnets, electronic inductors, transformers, magnetic recording tapes, and radar-absorbing coatings (Goldman, 2006).

The structure of these oxides derives from that of spinel magnetite, with formula Fe$_3$O$_4$, which consists of a face-centered cubic (fcc) oxygen lattice where the iron cations occupy the tetrahedral (A) and octahedral (B) interstitial sites as follows: (Fe^{3+})$_A$[Fe^{2+}Fe^{3+}]$_B$O$_4$. The magnetization in such a lattice results from the antiferromagnetic Néel coupling between the paramagnetic cations located in the A and B sub-lattices, which are themselves ferromagnetically arranged in each sub-lattice. This structure is called the inverse spinel structure by opposition to the direct structure, in which the divalent and the trivalent cations are exclusively located in the A and the B sites, respectively (Smith and Wijn, 1961).

A small substitution of tetrahedrally coordinated paramagnetic cations by nonmagnetic cations increases the magnetization, as expected by the collinear ferrimagnetic Néel's theory, while a large substitution, usually greater than 50%, reduces it, according to the canted ferrimagnetic Yafet–Kittel–like theory (Yafet and Kittel, 1952). At the same time, for such a large substitution ratio, if the diamagnetic ions are simultaneously located in the A and B sites, the canting is weakened and the magnetization reduction is limited, which always leads to values suitable for applications (Hochepied et al., 2000; Ammar et al., 2004; Ammar et al., 2006). These substitutions also affect the Curie temperature, T_C. Indeed, T_C is closely related to the number of bonds between paramagnetic iron cations through oxygen anions per formula unit (Gilleo, 1960). This number decreases when diamagnetic cations are introduced into the spinel lattice, whatever their location into the lattice, reducing the T_C value (Hanini et al., 2016).

The introduction into the structure of paramagnetic cations susceptible to be strongly affected by a spin–orbit coupling, such as Co^{2+} cations in B sites, increases the magnetocrystalline anisotropy of the resulting oxide, and consequently its coercivity. Reversely, a coordination change of these Co^{2+} cations results in its decrease. In other words, the strength of the spin–orbit coupling can be modulated by the concentration of octahedrally coordinated Co^{2+} cations (Smith and Wijn, 1961). From a thermodynamic point of view, Co^{2+} cations have a strong preference for a high-spin six-coordination in a regular octahedral oxygen-ligand crystal field. For this reason, bulk $CoFe_2O_4$ usually adopts the inverse spinel structure and has a large magnetocrystalline anisotropy energy constant [$K_1 = 1.2$ $10^3 kJ m^{-3}$ at 300 K (Smith and Wijn, 1961)]. However, this structure may deviate when nanocrystals are prepared by soft chemistry: the atomic ratio of Co^{2+} located in A sites being directly dependent on the operating synthesis conditions (Ammar et al., 2001; Artus et al., 2011). In general, the more they differ from the thermodynamic conditions, the greater the deviation, and conversely, the closer they are, the smaller the deviation (Pacakova et al., 2017). Even rare, the same trends have been observed in nickel ferrite nanoparticles. Indeed, while bulk $NiFe_2O_4$ adopts an exact inverse spinel structure, with a weak spin–orbit coupling on Ni^{2+} cations, nanocrystals do not adopt systematically. Depending on their synthesis conditions, they can present a nonzero concentration of tetrahedrally coordinated Ni^{2+} (Chkoundali et al., 2004; Beji et al., 2010) which results in a non-negligible spin–orbit coupling effect.

Polyol-made ferrite nanoparticles (NPs) are a good illustration of this relationship between the conditions of synthesis and the distribution of cations, and its consequence on the final magnetic properties (Caruntu et al., 2002; Ammar et al., 2004; Ammar et al., 2006; Hanini et al., 2016). In a standard synthesis, polyols act as solvents and complexing agents for metal ions, which subsequently react with a controlled amount of water or hydroxide to form the desired oxide phases. The polyols then offer favorable crystal growth conditions, thanks to their high boiling temperature and high viscosity, leading to well-crystallized and size-controlled oxide NPs. Thus, by varying the reaction temperature T (up to 325°C in tetraethyleneglycol) and the synthesis time (up to tens of hours), it would be possible to precipitate (Caruntu et al., 2002) or anneal (López-Ortega et al., 2020) fresh or preformed ferrite nanocrystals in polyols at different T and t values, thus tuning their final local structure and their magnetic properties.

Our purpose is to illustrate such a feature by focusing on polyol-made $NiFe_2O_4$ (NFO) NPs with particular attention to their post-polyol treatment. In practice, NFO NPs are prepared according to a well-established protocol, which consists of dissolving in a mixture of diethyleneglycol (the solvent) and water (the nucleophilic agent) metal acetate salts (in a stoichiometric atomic ratio), and heating the reaction solution under reflux for 3 h (see experiment section). A first part of the recovered particles is stored under vacuum for characterization, while a second part is dispersed in a fresh diethyleneglycol solvent and heated at a temperature of 180–200°C, overnight for a polyol-mediated annealing (a-NFO). All the prepared particles are then structurally characterized with a special emphasis on their cation distribution among the spinel lattice.
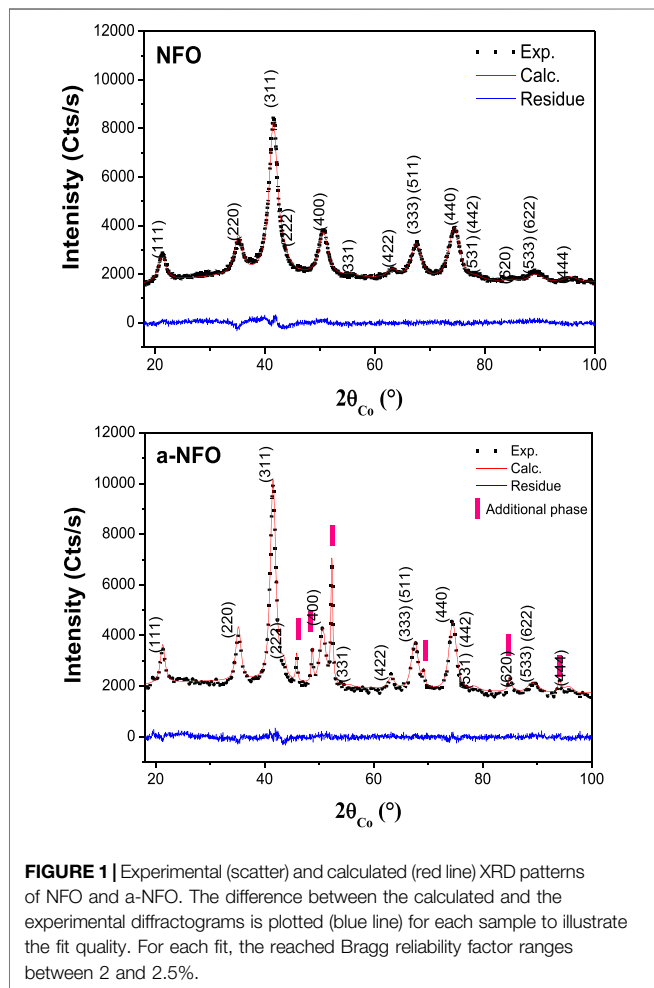
To achieve such a fine structural analysis, ^{57}Fe Mössbauer spectroscopy was chosen. As a local iron probe technique, it allows, thanks to its high sensitivity to the electronic state and the local chemical environment of iron species, identifying the oxidation state and the coordination of iron atom in any iron-based materials and particularly in nickel ferrites (Šepelák et al., 2007; Ahlawat et al., 2011; Mahmoud et al., 2013; Kurtan et al., 2016; Ushakov et al., 2017; Ushakov et al., 2018).

RESULTS AND DISCUSSION

The X-ray diffraction (XRD) pattern recorded on fresh NFO powder (**Figure 1**) corresponds very well to that of the nickel ferrite cubic spinel structure (ICDD n°98-002-8108), and conversely, that of the annealed one does not (**Figure 1**). It exhibits additional peaks assigned to a hexagonal Ni^0-based structure, either nickel metal (Carturan et al., 1988; Chinnasamy et al., 2005; Neiva et al., 2016) or nickel carbide Ni_3C (ICDD n° 98-001-7005). Both have the same XRD signature and have tabulated CIF files, but they crystallize in different unit cells: $a = 2.653$ nm and $c = 4.348$ nm for Ni (Carturan et al., 1988) and $a = 4.553$ nm and $c = 12.920$ nm for Ni_3C (Nagakura et al., 1958) within the $P6_3/mmc$ and R-3R space groups, respectively. This contaminant is very probably originated from Ni^{2+} cations, demixing from the spinel phase and their subsequent reduction in contact with the polyol solvent. Polyols are known as reducing agents for most of the d-transition metal cations (Fiévet et al., 2018). In such media, metals and metal carbides can be almost easily produced, depending on the operating conditions (Fiévet et al., 2018). Polyol chemists often assume that the reaction time is an important experimental issue. Based on the example of polyol-made cobalt and nickel carbides, by implementing the reaction for various times, it is assumed that carbide phases are formed through carbon (originated from surfactant or polyol itself thermal decomposition) diffusion into the initially produced metal crystals. Short polyol-mediated reduction reactions inhibit complete diffusion of carbon into the metal lattice and result in

TABLE 1 | Main structural and microstructural characteristics of NFO and a-NFO powders as deduced from XRD analysis. Typically the cell parameter, a; the average coherent diffraction domain size, <L$_{XRD}$>; and the weight content, wt. of each constituting phase are indicated.

	Spinel phase			Other phase		
	a (Å) ±0.005	<L$_{XRD}$> (nm) ±1	wt.−(%) ±10	a, c (Å) ±0.005	<L$_{XRD}$> (nm) ±1	wt.−(%) ±10
NFO	8.370	4	100	–	–	–
a-NFO	8.363	7	95	4.590, 13.001	36	5

FIGURE 1 | Experimental (scatter) and calculated (red line) XRD patterns of NFO and a-NFO. The difference between the calculated and the experimental diffractograms is plotted (blue line) for each sample to illustrate the fit quality. For each fit, the reached Bragg reliability factor ranges between 2 and 2.5%.

metal or metal carbide core-shell structures. Reversely, long reactions favor carbide stabilization instead of metal phase (Fujieda et al., 2012; Zamanpour et al., 2015; Fujieda et al., 2016), particularly if both the metal and the intermetallic crystallize in the same space group.

Rietveld refinement using MAUD software (Lutterotti et al., 1999) has thus been performed, assuming that NFO consists of a single NiFe$_2$O$_4$ phase, while a-NFO consists of a mixture of NiFe$_2$O$_4$ and Ni$_3$C phases. For each constituting phase, the cell parameters *a (and c)*, the average crystallographic coherence length <L$_{XRD}$> (assuming isotropic crystals), the average micro-deformation <ε>, and the weight ratio are

estimated and summarized in **Table 1**. Note that the atomic coordinates of all the atoms and their occupation site ratio in the spinel phase have been fixed during the fitting process. The close proximity of the electron numbers of Ni and Fe makes the refinement of these parameters irrelevant.

These values show clearly a small decrease in the cell parameter and a small increase in the average crystal size, for the spinel phase, suggesting composition variation and crystal growth during annealing.

Transmission and scanning transmission electron microscopy (TEM and STEM), operating in bright field (BF) or high-angle annular dark-field imaging (HAADF) modes, were performed to compare the morphology of the two sets of particles and to check carbide precipitation. Interestingly, the recorded micrographs evidence a slight ferrite particle size increase in a-NFO (~6 vs. 3 nm as shown in **Figure 2** and **Supplementary Figure S1**) as well its contamination with large nickel rich crystals (up to 100 nm in size) whose electron diffraction pattern matches very well with the hexagonal Ni$_3$C structure (**Figure 3**). Elemental mapping confirmed these features (see **Supplementary Figures S2, S3**), meaning that an important cation migration proceeds during the polyol-mediated annealing, while the total Fe/Ni atomic ratio in the two powders remains constant, equal to 2, as inferred from X-ray fluorescence spectroscopy (XRF). This means that NFO particles are certainly consistent with stoichiometric nickel ferrite oxide, while the a-NFO ones are not.

To rule out this idea, ^{57}Fe Mössbauer spectrometry was carried out as a tool for the local structural analysis of the spinel phase exclusively. The spectra were recorded at 300 and 77 K on the fresh and annealed samples, respectively (**Figure 4**). For both samples, the spectra at 300 K consist of a single broadened and slightly asymmetrical line, which can be well described by a single Lorentzian contribution. The refined isomer shift values are typical of Fe^{3+} species, and hyperfine structures are a consequence of superparamagnetic relaxation phenomena. It is important to conclude at this stage that the annealed sample does contain larger grains and/or more aggregated grain structures, consistent with a slowing down of superparamagnetic fluctuations. These phenomena persist even at 77 K for the two samples, but the spectra recorded at this low temperature differ somewhat from one sample to another. Indeed, that of NFO consists of a sextet with asymmetrically broadened lines, fitted assuming Lorentzian functions and using a pure discrete distribution of hyperfine field correlated linearly with that of the isomer shift, with values characteristics of ferric species. Such a hyperfine structure is most probably the result of a distribution of size of noninteracting and/or weakly interacting ferrite NPs,
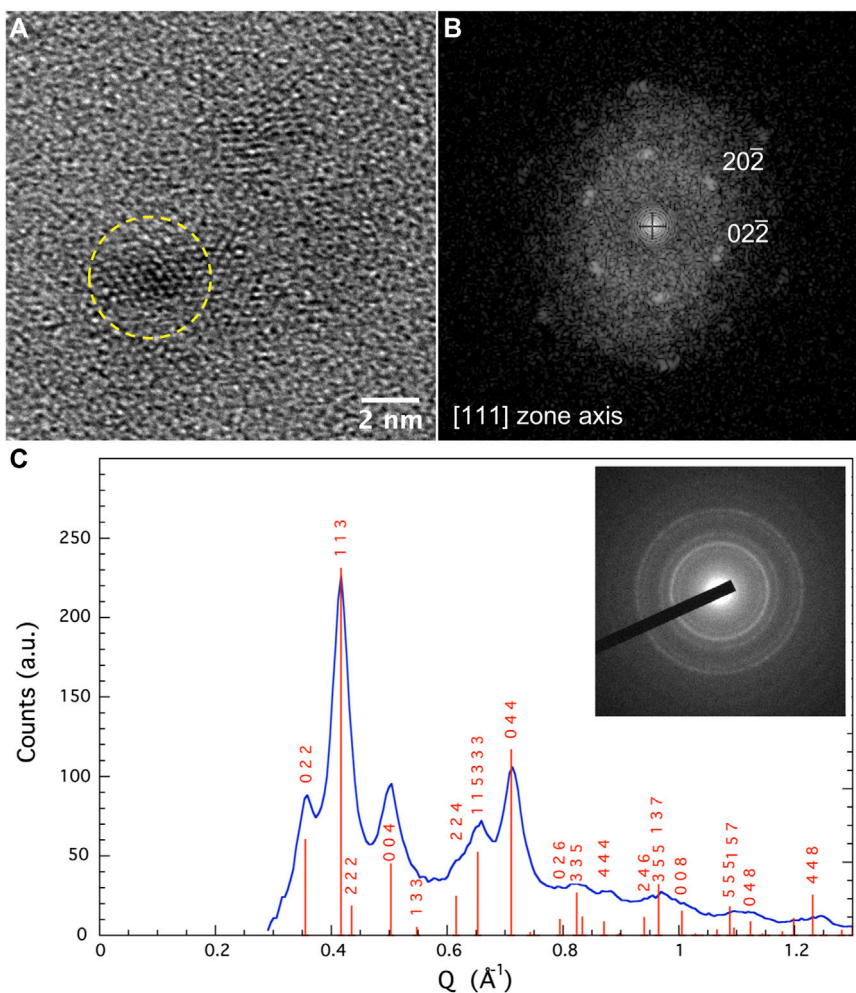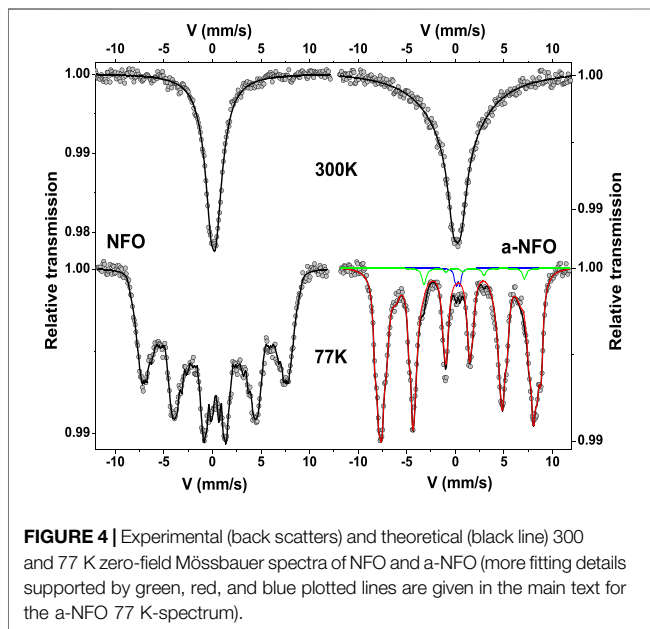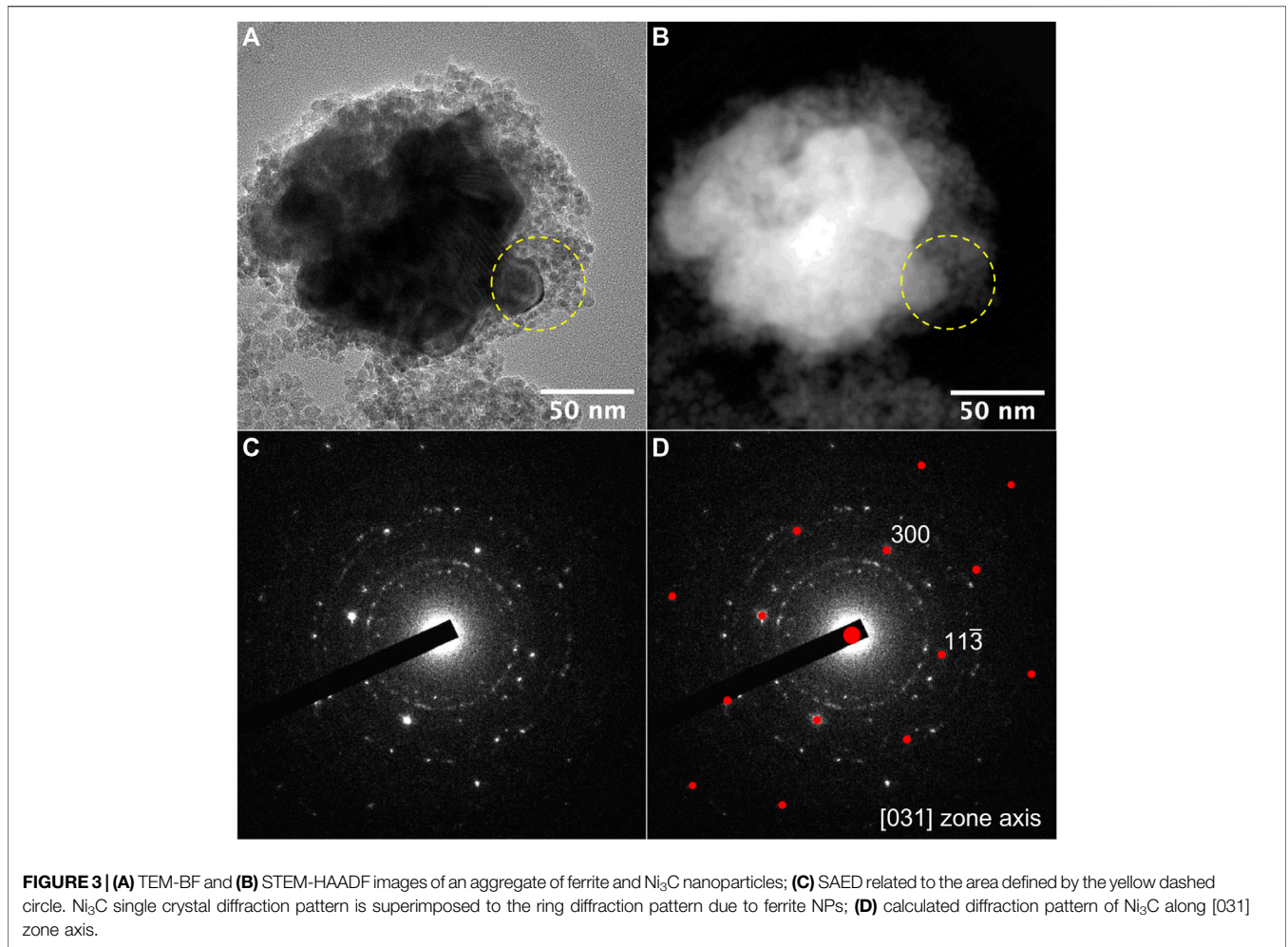
FIGURE 2 | (A) TEM-BF images of ferrite nanoparticles; **(B)** the fast Fourier transform (FFT) pattern recorded on a representative one fully indexed within the $NiFe_2O_4$ structure along [111] zone axis; **(C)** selected area electron diffraction (SAED) pattern related to the same observed region. The recorded diffraction rings match very well with the spinel structure.

the larger ones being already magnetically blocked, while the smaller ones being not. The lack of resolution prevents a definitive quantitative estimation of the relative proportions of each type of iron species, nor of their respective hyperfine field values (Greneche, 2013). Reversely, that of a-NFO exhibits a much more resolved hyperfine structure fitted assuming a prevailing magnetic sextet (96 at-Fe %; red color) attributed to blocked and rather blocked Fe^{3+} magnetic moments, a small quadrupolar doublet (~1 at-Fe %; blue) corresponding to fluctuating Fe^{3+} magnetic moments probably located in the smallest in size particles and a single magnetic sextet (~3 at-Fe %; green) attributed to Fe^{2+} magnetic moments. These results suggest a slight size increase between NFO and a-NFO ferrite crystals as well a reduction of a very small proportion of ferric cations into ferrous ones during the annealing step.
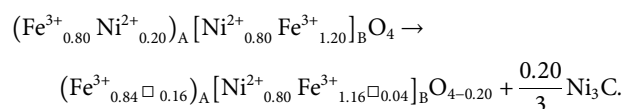
An external magnetic field of 8 T at 12 K was then applied parallel to the γ-beam, giving rise to split the sextet into two well-resolved sextets according to the ferrimagnetic structure, and the

recorded spectra on all the samples are compared in **Figure 5**. As expected, both consist of the superposition of two sextets attributed to octahedrally and tetrahedrally coordinated Fe^{3+} cations. The refined values of the hyperfine parameters are listed in **Table 2**, emphasizing a total absence of ferrous cations in both samples. The introduced small Fe^{2+} component in the fitting model of the a-NFO 77 K spectrum is thus not relevant at all. Interestingly, both samples exhibit the same A and B sites occupancy by the ferric cations, in agreement with a departure from the thermodynamically stable inverse spinel structure. A small decrease can also be noticed in the B_{hf} hyperfine field values when comparing the annealed sample with the fresh one, certainly suggesting a chemical or structural variation on the A and B atomic populations (**Table 2**) and, last but not least, a clear increase in the spin canting angles θ of the magnetic ferric species concerned.

To tentatively understand what is happening in the annealed sample, one has to remember that nickel demixing has occurred.

FIGURE 3 | **(A)** TEM-BF and **(B)** STEM-HAADF images of an aggregate of ferrite and Ni_3C nanoparticles; **(C)** SAED related to the area defined by the yellow dashed circle. Ni_3C single crystal diffraction pattern is superimposed to the ring diffraction pattern due to ferrite NPs; **(D)** calculated diffraction pattern of Ni_3C along [031] zone axis.

FIGURE 4 | Experimental (back scatters) and theoretical (black line) 300 and 77 K zero-field Mössbauer spectra of NFO and a-NFO (more fitting details supported by green, red, and blue plotted lines are given in the main text for the a-NFO 77 K-spectrum).

TEM and XRD show clearly that some of the nickel atoms depart from the spinel phase to precipitate in a foreign phase. One explanation is that the ferrite phase in a-NFO is much more consistent with a nonstoichiometric spinel oxide, in which the departure of Ni^{2+} from the A sites is compensated by a rearrangement of the ferric cations: this leads to the stabilization of cation and anion vacancies, to compensate the positive charge loss. As a first approximation, it is assumed that cation vacancies are located in the octahedral spinel sub-lattice rather than in the tetrahedral one. These rearrangements in the spinel phase are accompanied by the precipitation of an equivalent amount of Ni^0 in the form of nickel carbide:

$$\left(Fe^{3+}_{0.80} Ni^{2+}_{0.20}\right)_A \left[Ni^{2+}_{0.80} Fe^{3+}_{1.20}\right]_B O_4 \rightarrow$$

$$\left(Fe^{3+}_{0.84} \square_{0.16}\right)_A \left[Ni^{2+}_{0.80} Fe^{3+}_{1.16} \square_{0.04}\right]_B O_{4-0.20} + \frac{0.20}{3} Ni_3C.$$

The 6.6 wt-% (namely, 5.3 wt-%) of Ni_3C deduced from the Mössbauer refinement agreed very well with the 5 wt-% measured by XRD on the annealed sample.
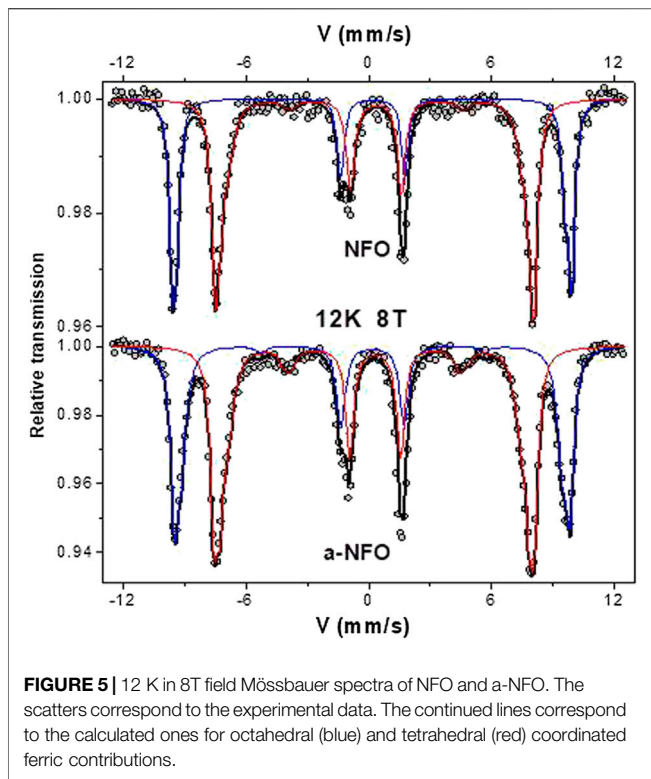
FIGURE 5 | 12 K in 8T field Mössbauer spectra of NFO and a-NFO. The scatters correspond to the experimental data. The continued lines correspond to the calculated ones for octahedral (blue) and tetrahedral (red) coordinated ferric contributions.

Indeed, using the ferric occupation ratios of the A and B sites in a-NFO and applying **Eq. 1**, in which M_{spinel} and $M_{carbide}$ are the molar weight of the new spinel and carbide phases, respectively, lead to a ferrite weight content of 95 wt-%, which is in good agreement with the value inferred from XRD analysis (see **Table 1**):

$$wt. - \% \left(spinel\right) = 100 \times \frac{M_{spinel}}{M_{spinel} + \left(\frac{x}{3} \times M_{carbide}\right)}. \quad (1)$$

To strengthen these hypotheses, one has to consider the B_{hf} and θ values of the two samples and compare them from one sample to another. As mentioned earlier, the former decreases in the annealed sample, while the latter increases. Usually, from bulk magnetite, nickel substitution tends to replace preferentially iron in octahedral coordination and increases the B_{hf} value of octahedrally coordinited ferric iron (Lelis et al., 2003). We observe exactly the opposite, a decrease of A and B B_{hf} in the annealed sample, as a consequence of nickel depletion. Moreover, the cation vacancies are in agreement with a local canting

increase. Also, θ is significantly higher in the annealed sample for both the octahedrally and tetrahedrally coordinated ferric cations (**Table 2**).

The concentration of oxygen vacancies in the final ferrite oxide is not so critical. The nonstoichiometry of oxygen is often reported in fine-grained ferrites submitted to a subsequent gaseous (reducing or oxidative) annealing (Guillemet-Fritsch et al., 1999; Gillot and Tailhades, 2000; Antic et al., 2004; Kremenovic et al., 2005; Beji et al., 2015). It is compensated by cationic mixed valence states and/or cation vacancies, which may contribute to the enhancement of the iron magnetic moment canting.

The observed cation migration phenomenon, mediated by polyol annealing, has already been reported on granular hetero-nanostructures based on cobalt ferrite. In this case, no cobalt depletion was reported, but there is an evolution of the spinel structure from a deviated structure to an exact inverse one after heating in polyol overnight in the presence of cobalt salts to form $CoFe_2O_4@CoO$ core@shell NPs (Flores-Martinez et al., 2018). Most probably, depletion was avoided, thanks to a complex migration pathway involving both $CoFe_2O_4$ (seeds) and CoO (deposits) phases. Cation migration was also observed during prolonged air annealing of polyol-made nickel–zinc ferrite NPs (Beji et al., 2010). Whereas Ni^{2+}, Zn^{2+}, and Fe^{3+} cations occupied both the tetrahedral and octahedral sites of the spinel lattice in the as-prepared NPs, the annealed ones exhibit a decreasing concentration of tetrahedrally coordinated Ni^{2+} and octahedrally coordinated Zn^{2+} cations, leading at the end to the thermodynamically stable $(Fe^{3+}_{1-x}Zn^{2+}_x)_A[Fe^{3+}_{1+x}Ni^{2+}_{1-x}]_BO_4$ structure (Beji et al., 2010).

CONCLUSION

From well-crystallized and ultrafine $NiFe_2O_4$ NPs, prepared by the polyol route, we have shown that due to their relatively soft synthesis conditions, they exhibit a local structure which deviates from the thermodynamically stable inverse structure with about 20 wt-% of the involved nickel atoms located in the tetrahedral A sites. We have also shown that a polyol-mediated annealing process applied to these NPs leads to a slight increase of their average size accompanied by a non-negligible change of their chemical composition and structure, leading to the stabilization of nonstoichiometric $(Fe^{3+}_{0.84}\square_{0.16})_A$ $[Ni^{2+}_{0.80}Fe^{3+}_{1.16}\square_{0.04}]_BO_{4-0.20}$ ferrite as a consequence of cation migration and particularly nickel demixing. The initially tetrahedrally coordinated nickel cations demix from the spinel

TABLE 2 | The isomer shift (δ), the quadrupole shift (2ε), the effective field (B_{eff}), the hyperfine field (B_{hf}), the average canting angle (ϑ), and the ratio of each component evaluated from in-field Mössbauer fitted spectra are reported for NFO and a-NFO.

	Site	$<\delta>$ (mm/s)	$<2\varepsilon>$ (mm/s)	$<B_{eff}>$ (T)	$<B_{hf}>$ (T)	$<\theta>$ (°)	*Ratio* (at%)
		±0.01	±0.01	±0.2	±0.2	±10°	±1
NFO	Fe^{3+}_A	0.33	−0.00	59.7	51.7	0	40
	Fe^{3+}_B	0.48	−0.00	47.5	55.4	7	60
a-NFO	Fe^{3+}_A	0.33	−0.03	58.7	50.9	13	42
	Fe^{3+}_B	0.46	−0.03	46.4	53.8	24	58

lattice, precipitating as a foreign nickel carbide phase, depending on the electropositivity of the nickel atoms themselves and the reducing capability of the polyol itself. These results highlight how the local structure of soft chemistry–made ferrite NPs is versatile and how it can easily evolve by acting on their in-solution synthesis and/or annealing conditions without varying significantly their average crystal size.

Experiments

Chemicals. $Fe(CH_3CO_2)_2$ and $Ni(CH_3CO_2)_2.4H_2O$ metal salt precursors, and $HO(CH_2)_2O(CH_2)_2OH$ (DEG, b.p. = 245°C) solvent were purchased from ACROS and used without purification.

Particles preparation. An appropriate amount of metal salts was dissolved in a mixture of water in DEG using a three-neck flask. The hydrolysis ratio h (defined as the ratio between water quantity and metal cation quantity) was fixed to $h = 24$, which is the best value for the preparation of ultrafine highly crystalline nickel ferrite NPs. The solution was heated to boiling (155°C) and maintained under reflux for 3 h. After cooling to room temperature, the particles were separated by centrifugation, washed with ethanol, and then dried in air at 50°C. A part of these particles was dispersed in a fresh DEG solvent and heated under reflux for 12 h at 180°C to form a-NFO.

Structural characterization. The chemical composition of the produced powders was checked by XRF. The Fe and Ni atomic contents were analyzed by using certified solutions with appropriate Fe and Ni composition on a Panalytical Epsilon 3XL spectrometer equipped with an Ag X-ray tube operating at 30 kV and 480 μA current emissions. Their crystalline structure was checked by XRD using a Panalytical X'pert Pro diffractometer, working in the Bragg–Brentano θ-2θ reflexion geometry, and equipped with a multichannel X'celerator detector and a cobalt X-ray tube operating at 40 kV and 40 mA. Rietveld refinements were then performed using a pseudo-Voigt and a polynomial function to, respectively, model the peak profile and the background. These measurements were complemented by [57]Fe Mössbauer spectrometry, performed at 300 and 77 K in a zero magnetic field, and at 12 K in a 8 T magnetic field oriented parallel to the γ-beam. A [57]Co/Rh γ-ray source with an activity of about 1.5 GBq and mounted on a conventional constant acceleration vibrating electromagnetic transducer was used. The samples consist of a homogeneous layer of powder containing about 5 mg of Fe/cm^2. The calibration is obtained using an α-Fe foil, and the values of isomer shift were referred to those of α-Fe at 300 K. The Mössbauer spectra were described by a superposition of quadrupolar and/or magnetic components composed of Lorentzian lines, and the values of the hyperfine parameters were refined using the Mosfit program (Teillet and Varret, 1983) based on a least square method and a diagonalization of the Hamiltonian. In parallel, TEM observations were performed on all the samples using a JEOL 2100F microscope (200 kV) equipped with a Schottky emission gun, a high-resolution UHR pole piece, and a Gatan US4000 CCD camera.

DATA AVAILABILITY STATEMENT

The original contributions presented in the study are included in the article/**Supplementary Material**; further inquiries can be directed to the corresponding author.

AUTHOR CONTRIBUTIONS

TG: data curation and formal analysis; ZN: data curation and formal analysis; SN: experimental support; NM: experimental support, formal analysis and scientific discussion; NY: experimental support, formal analysis, and writting—review; J-MG: experimental support, formal analysis, and writting—review; SA: research supervision, project administration, and writing—review.

FUNDING

SUPPLEMENTARY MATERIAL

The Supplementary Material for this article can be found online at: https://www.frontiersin.org/articles/10.3389/fmats.2021.668994/full#supplementary-material

REFERENCES

Ahlawat, A., Sathe, V. G., Reddy, V. R., and Gupta, A. (2011). Mossbauer, Raman and X-ray Diffraction Studies of Superparamagnetic NiFe2O4 Nanoparticles Prepared by Sol-Gel Auto-Combustion Method. *J. Magnetism Magn. Mater.* 323, 2049–2054. doi:10.1016/j.jmmm.2011.03.017

Ammar, S., Helfen, A., Jouini, N., Fiévet, F., Rosenman, I., Villain, F., et al. (2001). Magnetic Properties of Ultrafine Cobalt Ferrite Particles Synthesized by Hydrolysis in a Polyol Medium. *J. Mater. Chem.* 11, 186–192. doi:10.1039/b003193n

Ammar, S., Jouini, N., Fiévet, F., Beji, Z., Smiri, L., Moliné, P., et al. (2006). Magnetic Properties of Zinc Ferrite Nanoparticles Synthesized by Hydrolysis in a Polyol Medium. *J. Phys. Condens. Matter* 18, 9055–9069. doi:10.1088/0953-8984/18/39/032

Ammar, S., Jouini, N., Fiévet, F., Stephan, O., Marhic, C., Richard, M., et al. (2004). Influence of the Synthesis Parameters on the Cationic Distribution of ZnFe2O4 Nanoparticles Obtained by Forced Hydrolysis in Polyol Medium. *J. Non-Crystalline Sol.* 345-346, 658–662. doi:10.1016/j.jnoncrysol.2004.08.162

Antic, B., Kremenović, A., Nikolic, A. S., and Stoiljkovic, M. (2004). Cation Distribution and Size-Strain Microstructure Analysis in Ultrafine Zn–Mn Ferrites Obtained from Acetylacetonato Complexes. *J. Phys. Chem. B* 108, 12646–12651. doi:10.1021/jp036214v

Artus, M., Ben Tahar, L., Herbst, F., Smiri, L., Villain, F., Yaacoub, N., et al. (2011). Size-dependent Magnetic Properties of CoFe2O4 nanoparticles Prepared in Polyol. *J. Phys. Condens. Matter* 23, 506001. doi:10.1088/0953-8984/23/50/506001

Beji, Z., Smiri, L. S., Yaacoub, N., Grenèche, J.-M., Menguy, N., Ammar, S., et al. (2010). Annealing Effect on the Magnetic Properties of Polyol-Made Ni–Zn Ferrite Nanoparticles. *Chem. Mater.* 22, 1350–1366. doi:10.1021/cm901969c

Beji, Z., Sun, M., Smiri, L. S., Herbst, F., Mangeney, C., and Ammar, S. (2015). Polyol Synthesis of Non-stoichiometric Mn-Zn Ferrite Nanocrystals: Structural/microstructural Characterization and Catalytic Application. *RSC Adv.* 5, 65010–65022. doi:10.1039/c5ra07562a

Carturan, G., Cocco, G., Enzo, S., Ganzerla, R., and Lenarda, M. (1988). Hexagonal Close Packed Nickel Powder: Synthesis, Structural Characterization and Thermal Behavior. *Mater. Lett.* 7, 47–50. doi:10.1016/0167-577X(88)90080-8

Caruntu, D., Remond, Y., Chou, N. H., Jun, M.-J., Caruntu, G., He, J., et al. (2002). Reactivity of 3d Transition Metal Cations in Diethylene Glycol Solutions. Synthesis of Transition Metal Ferrites with the Structure of Discrete Nanoparticles Complexed with Long-Chain Carboxylate Anions. *Inorg. Chem.* 41, 6137–6146. doi:10.1021/ic025664j

Chinnasamy, C. N., Jeyadevan, B., Shinoda, K., Tohji, K., Narayanasamy, A., Sato, K., et al. (2005). Synthesis and Magnetic Properties of Face-Centered-Cubic and Hexagonal-Close-Packed Ni Nanoparticles through Polyol Process. *J. Appl. Phys.* 97, 10J309. doi:10.1063/1.1851951

Chkoundali, S., Ammar, S., Jouini, N., Fiévet, F., Molinié, P., Danot, M., et al. (2004). Nickel Ferrite Nanoparticles: Elaboration in Polyol Medium via Hydrolysis, and Magnetic Properties. *J. Phys. Condens. Matter* 16, 4357–4372. doi:10.1088/0953-8984/16/24/017

Fiévet, F., Ammar-Merah, S., Brayner, R., Chau, F., Giraud, M., Mammeri, F., et al. (2018). The Polyol Process: a Unique Method for Easy Access to Metal Nanoparticles with Tailored Sizes, Shapes and Compositions. *Chem. Soc. Rev.* 47, 5187–5233. doi:10.1039/c7cs00777a

Flores-Martinez, N., Franceschin, G., Gaudisson, T., Beaunier, P., Yaacoub, N., Greneche, J.-M., et al. (2018). Giant Exchange-Bias in Polyol-Made CoFe2 O4 -CoO Core-Shell Like Nanoparticles. *Part. Part. Syst. Charac.* 35, 1800290. doi:10.1002/ppsc.201800290

Fujieda, S., Shinoda, K., Suzuki, S., and Jeyadevan, B. (2012). Synthesis of Ni Carbide Nanoparticles with Ni3C-type Structure in Polyol Solution Containing Dispersant. *Mater. Trans.* 53, 1716–1720. doi:10.2320/matertrans.m2012160

Fujieda, S., Yomogida, A., Shinoda, K., and Suzuki, S. (2016). *IEEE Magn. Lett.* 7, 2107104. doi:10.1109/lmag.2016.2610581

Gilleo, M. A. (1960). Superexchange Interaction in Ferrimagnetic Garnets and Spinels Which Contain Randomly Incomplete Linkages. *J. Phys. Chem. Sol.* 13, 33–39. doi:10.1016/0022-3697(60)90124-4

Gillot, B., and Tailhades, P. (2000). Temperature Dependence of Oxidation Behavior and Coercivity Evolution in fine-grained Spinel Ferrites. *J. Magnetism Magn. Mater.* 208, 181–187. doi:10.1016/s0304-8853(99)00591-0

Goldman, A. (2006). "Applications and Functions of Ferrites," in *Modern Ferrite Technology*. Boston: Springer.

Greneche, J.-M. (2013). "The Contribution of 57Fe Mössbauer Spectrometry to Investigate Magnetic Nanomaterials," in *Mössbauer Spectroscopy*. Editors Y. Yoshida and G. Langouche (Berlin Heidelberg: Springer), 187–241.

Guillemet-Fritsch, S., Viguié, S., and Rousset, A. (1999). Structure of Highly Divided Nonstoichiometric Iron Manganese Oxide Powders Fe3−xMnx3δ/ 4O4+δ. *J. Solid State. Chem.* 146, 245–252. doi:10.1006/jssc.1999.8345

Hanini, A., Lartigue, L., Gavard, J., Kacem, K., Wilhelm, C., Gazeau, F., et al. (2016). Zinc Substituted Ferrite Nanoparticles with Zn0.9Fe2.1O4 Formula Used as Heating Agents for *In Vitro* Hyperthermia Assay on Glioma Cells. *J. Magnetism Magn. Mater.* 416, 315–320. doi:10.1016/j.jmmm.2016.05.016

Hochepied, J. F., Bonville, P., and Pileni, M. P. (2000). Nonstoichiometric Zinc Ferrite Nanocrystals: Syntheses and Unusual Magnetic Properties. *J. Phys. Chem. B* 104, 905–912. doi:10.1021/jp991626i

Kremenovic, A., Antic, B., Spasojevic, V., Vucinic-Vasic, M., Jaglicic, Z., Pirnat, J., et al. (2005). X-ray Powder Diffraction Line Broadening Analysis and Magnetism of Interacting Ferrite Nanoparticles Obtained from Acetylacetonato Complexes. *J. Phys. Condens. Matter* 17, 4285–4299. doi:10.1088/0953-8984/17/27/005

Kurtan, U., Güngüneş, H., Sözeri, H., and Baykal, A. (2016). Synthesis and Characterization of Monodisperse NiFe2O4 Nanoparticles. *Ceramics Int.* 42, 7987–7992. doi:10.1016/j.ceramint.2016.01.200

Lelis, M. d. F. F., Fabris, J. D., Mussel, W. d. N., and Takeuchi, A. Y. (2003). Preparation and Characterization of Nickel-And Cobalt-Doped Magnetites. *Mat. Res.* 6, 145–150. doi:10.1590/s1516-14392003000200006

López-Ortega, A., Muzzi, B., Lottini, E., Peddis, D., Bertoni, G., de Julián Fernández, C., et al. (2020). "Improving the Permanent Magnetic Properties of Cobalt Ferrite Nanoparticles by a Controlled Solvent-Mediated Annealing Process," in 28th Conference of the Condensed Matter Joint with the Biennial Meeting of the Condensed Matter Divisions of the Spanish. Royal Physics Society and of the European Physical Society - CMD2020 GEFES, Madrid, Spain, August 31–September 4, 2020.

Lutterotti, L., Matthies, S., and Wenk, H. R. (1999). MAUD: a friendly Java program for material analysis using diffraction. *IUCr CPD Newslett.* 21, 14.

Mahmoud, M. H., Elshahawy, A. M., Makhlouf, S. A., and Hamdeh, H. H. (2013). Mössbauer and Magnetization Studies of Nickel Ferrite Nanoparticles Synthesized by the Microwave-Combustion Method. *J. Magnetism Magn. Mater.* 343, 21–26. doi:10.1016/j.jmmm.2013.04.064

Nagakura, S. (1958). Study of Metallic Carbides by Electron Diffraction Part II. Crystal Structure Analysis of Nickel Carbide. *J. Phys. Soc. Jpn.* 13, 1005–1014.

Néel, M. L. (1948). Propriétés magnétiques des ferrites ; ferrimagnétisme et antiferromagnétisme. *Ann. Phys.* 12, 137–198. doi:10.1051/anphys/194812030137

Neiva, G. C. E., Oliveira, M. M., Marcolino, L. H., and Zarbin, A. J. G. (2016). Nickel Nanoparticles with hcp Structure: Preparation, Deposition as Thin Films and Application as Electrochemical Sensor. *J. Colloid Interface Sci.* 468, 34–41. doi:10.1016/j.jcis.2016.01.036

Pacakova, B., Kubickova, S., Reznickova, A., Niznansky, D., and Vejpravova, J. (2017). "Spinel Ferrite Nanoparticles: Correlation of Structure and Magnetism," in *Magnetic Spinels - Synthesis, Properties And Applications*. Editors M. Seehra (London: IntechOpen). doi:10.5772/66074

Šepelák, V., Bergmann, I., Feldhoff, A., Heitjans, P., Krumeich, F., Menzel, D., et al. (2007). Nanocrystalline Nickel Ferrite, NiFe2O4: Mechanosynthesis, Nonequilibrium Cation Distribution, Canted Spin Arrangement, and Magnetic Behavior. *J. Phys. Chem. C* 111, 5026–5033. doi:10.1021/jp067620s

Smith, S., and Wijn, H. P. J. (1961). *Ferrites*. Amsterdam: Philips Library.

Teillet, J., and Varret, F. (1983). *Unpublished MOSFIT Program*. Le Mans (France): Le Mans Université.

Ushakov, M. V., Oshtrakh, M. I., Chukin, A. V., Šepelák, V., Felner, I., and Semionkin, V. A. (2018). *Hyperfine Interact* 239, 4. doi:10.1007/s10751-017-1478-7

Ushakov, M. V., Senthilkumar, B., Kalai Selvan, R., Felner, I., and Oshtrakh, M. I. (2017). Mössbauer Spectroscopy of NiFe2O4 Nanoparticles: The Effect of Ni 2+ in the Fe 3+ Local Microenvironment in Both Tetrahedral and Octahedral Sites. *Mater. Chem. Phys.* 202, 159–168. doi:10.1016/j.matchemphys.2017.09.011

Yafet, Y., and Kittel, C. (1952). Antiferromagnetic Arrangements in Ferrites. *Phys. Rev.* 87, 290–294. doi:10.1103/physrev.87.290

Zamanpour, M., Bennett, S. P., Majidi, L., Chen, Y., and Harris, V. G. (2015). Process Optimization and Properties of Magnetically Hard Cobalt Carbide Nanoparticles via Modified Polyol Method. *J. Alloys Comp.* 625, 138–143. doi:10.1016/j.jallcom.2014.11.083